

Magneto-optical response of chromium trihalide monolayers: chemical trends

Alejandro Molina-Sánchez,^{*,†} Gonçalo Catarina,[†] Davide Sangalli,[‡] and Joaquín Fernández-Rossier^{*,†}

[†]*QuantaLab, International Iberian Nanotechnology Laboratory (INL), Avenida Mestre José Veiga, 4715-330 Braga, Portugal*

[‡]*Istituto di Struttura della Materia, Consiglio Nazionale delle Ricerche (CNR-ISM), Division of Ultrafast Processes in Materials (FLASHit), Via Salaria Km 29.5, CP 10, I-00016 Monterotondo Stazione, Italy*

E-mail: alejandro.molina@uv.es

^aOn permanent leave from Departamento de Física Aplicada, Universidad de Alicante, San Vicente del Raspeig, 03690 Spain

Abstract

Chromium trihalides (CrI_3 , CrBr_3 and CrCl_3) form a prominent family of isostructural insulating layered materials in which ferromagnetic order has been observed down to the monolayer. Here we provide a comprehensive computational study of magneto-optical properties that are used as probes for the monolayer ferromagnetic order: magnetic circular dichroism and magneto-optic Kerr effect. Using a combination of density functional and Bethe-Salpeter theories, we calculate both the optical absorption and the magneto-optical Kerr angle spectra, including both excitonic effects and spinorial wave functions. We compare the magneto-optical response of the chromium trihalides series and we find that its strength is governed by the spin-orbit coupling of the ligand atoms (I, Br, Cl).

Introduction

The family of chromium trihalides plays a very prominent role in the research area of magnetic 2D crystals. Ferromagnetic order down to the monolayer in a stand-alone 2D crystal was first reported for a CrI_3 sample, back in 2017.^{1,2} This discovery triggered an intensive research that has led to the discovery of ferromagnetic order in monolayers and few layers of several compounds,^{3,4} including CrBr_3 ,^{5,6} CrCl_3 ⁷ and many others.⁸⁻¹⁰ The fabrication of Van der Waals heterostructures integrating these newly discovered 2D ferromagnets with other 2D crystals¹¹ has further fueled this research area and has motivated several theory proposals of new spintronic devices^{12,13} and topological phases.¹⁴

Magneto-optical probes, such as Kerr effect and magnetic circular dichroism (MCD), are widely used to probe the existence of ferromagnetic order in monolayers,^{1,15-19} as well as to probe the valley polarization²⁰ and magnetic proximity effects.²¹ The detection limit of conventional SQUID magnetometry, down to $10^{12} \mu_B$,²² sets a lower limit for the area of the monolayers in the range of $(100 \mu m)^2$, whereas the typical flakes have linear dimensions smaller than $10 \mu m$.

Both the Kerr angle and MCD can be related to the transverse (Hall) ac conductivity of the compounds, $\sigma_{xy}(\omega)$.²³⁻²⁵ At the microscopic level, this quantity arises from Lorentz-type forces acting on the electrons. In the absence of an external magnetic field, σ_{xy} is only non-zero when both spin-orbit interaction and the breaking of time reversal symmetry, inherent in the ferromagnetic order, are present.²⁶ Spin-orbit coupling is also essential in magnetic 2D crystals as it brings magnetic anisotropy, that ensures the existence of magnetic order in two dimensions. In the case of CrI_3 it has been demonstrated that it is the spin-orbit coupling of the ligand, the iodine atom, the one that controls magnetic anisotropy.²⁷

So far, theoretical efforts have been focused on the excitonic effects on Kerr angle in monolayer CrI_3 ,²⁸ or few-layers and bulk.²⁵ Others *ab initio* studies have described magnetic anisotropy and critical temperatures of ferromagnetic 2D materials,^{29,30} localized surface waves in CrI_3 structures,³¹ and structural properties.³² Nevertheless, a theoretical study

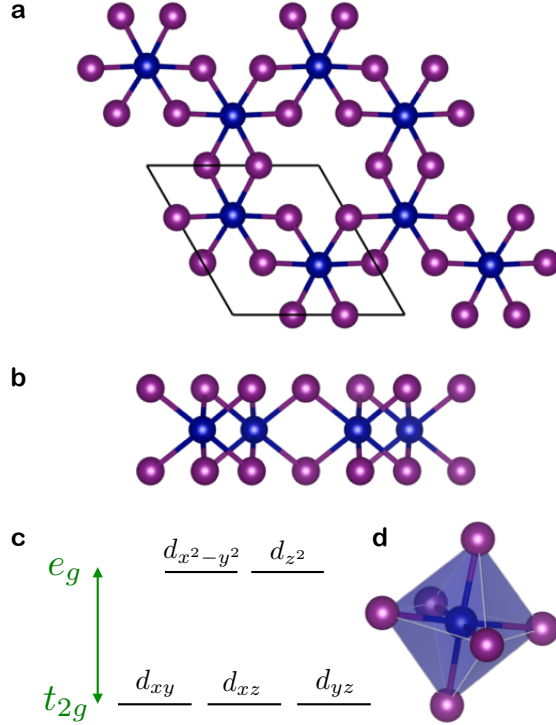


Figure 1: Crystalline structure of monolayer chromium trihalides (point symmetry D_{3d}). (a-b) Top and lateral view. (c-d) Scheme of the energy alignment of Cr d -orbitals as a result of the crystal-field splitting produced by the distortion of the octahedral environment.

focused on the chemical trends of the magneto-optical properties of the family of chromium trihalides, including excitonic effects, is still missing.

With this background, it is natural to enquire which atom, either Cr or the ligand, provides the spin-orbit interaction that controls the magnet in the CrX_3 family, with $\text{X}=\text{I}, \text{Br}, \text{Cl}$. Therefore, here we undertake an *ab initio* study of the chromium trihalide family. Our methodology includes a density functional theory (DFT) calculation to obtain ground state properties, extended with a GW and Bethe Salpeter calculation to compute the optical response, including the interplay between magnetism and spin-orbit coupling. These methods, that permit to fully include the excitonic effects, known to be very strong in 2D crystals, have been employed to study the CrI_3 monolayers in a recent publication.²⁸ Our work permits to carry out a comparative analysis of the optical and magneto-optical response of the CrX_3 series.

Methods

Ab initio and many-body perturbation theory

In this section we briefly describe the *ab initio* methodology used to compute the ground state properties of the CrX_3 and their optical response. The *ab initio* calculations of the electronic structure of the monolayer CrI_3 , CrBr_3 and CrCl_3 have been performed using Quantum Espresso.³³ We have employed the local density approximation (LDA) plus on-site Hubbard correction with values $U = 1.5$ eV and Hund's exchange interaction $J = 0.5$ eV.³⁴ We have included spin-orbit interaction with spinorial wave functions, using norm-conserving fully relativistic pseudopotentials. The pseudopotentials of Cr atom include semi-core valence electrons and have been generated with ONCVSP³⁵ and PSEUDODOJO.³⁶ The electronic density converges with an energy cutoff of 87 Ry and a \mathbf{k} -grid of $12 \times 12 \times 1$. We use a slab model with a 20 Å vacuum thickness to avoid interactions between periodic images. Since LDA underestimated the bandgap, we compute the GW band-gap corrections on top of the LDA+U. Let us label (GW+U)(LDA+U) the final band-gap, since keep the U correction for the correlated d electrons, which is not accounted for by the GW self-energy, on top of GW. Other choices are of course possible, like for example the update of the U correction in the GW framework, or the removal of the U correction to the simpler scheme GW(LDA+U). A discussion on the differences between these approaches is however beyond the goal of the present manuscript.

In order to obtain a realistic optical response, we have included excitonic effects, fundamental in semiconducting 2D materials.³⁷ The excitonic effects are taken into account via the Bethe-Salpeter Equation (BSE) as implemented in Yambo.^{38,39} The excitonic spectra and the dielectric function has been converged with a \mathbf{k} -grid of $15 \times 15 \times 1$ and a dielectric cut-off of 5 Ry. The dynamical screening effect has been included using the plasmon-pole approximation.⁴⁰ Since GW corrections are computed only at the band-gap, we used a scissor operator to extrapolate them to the whole $15 \times 15 \times 1$ \mathbf{k} -grid in the BSE calculations. This

choice does not alter the final result (we have checked that the GW correction is a rigid-shift of the LDA electronic structure) but reduces considerably the computational effort. The Coulomb interaction is truncated by using the Coulomb cut-off technique.⁴¹ Finally we use the ‘‘Covariant approach’’³⁹ for the dipole matrix elements to account for the non local U term included in the DFT Hamiltonian. This is crucial to obtain correct intensities in the absorption and thus a correct estimation of the Kerr angles.

MCD and Kerr angle in terms of the dielectric tensor

An effective dielectric tensor is defined as

$$\varepsilon = 1 + \frac{4\pi\alpha_{2D}}{d}, \quad (1)$$

where α_{2D} is the polarizability per surface unit and d the 2D-material thickness. We have assumed a thickness $d_{CrX_3} = 0.66$ nm for all the monolayers. It is calculated with the Yambo code, including excitonic effects and local-field effects.³⁹ From the effective dielectric tensor we can define the absorbance for linearly (A_x) and circularly (A_{\pm}) polarized light as:^{42,43}

$$A_x = \Im(\varepsilon_{xx})\frac{\omega d}{c}, \quad A_{\pm} = \Im(\varepsilon_{xx} \pm i\varepsilon_{xy})\frac{\omega d}{c}, \quad (2)$$

which is independent from d and thus a property of the 2D material.

From the effective dielectric tensor we can also obtain the Kerr angle, defined as the change to light polarization reflected from a magnetized surface. The expression for the Kerr angle is derived using the standard Fresnel formalism, assuming normal incidence of linearly polarized light (polar geometry). In order to account for the effect of a substrate, we consider a stratified medium where the magnetic material, with thickness d_{CrX_3} , is placed between air and a semi-infinite dielectric substrate. In the case of SiO₂ substrate, the relative permittivity at the relevant frequencies is $\varepsilon_r = 2.4$.⁴⁴ The effective dielectric tensor of CrX_3 is diagonal due to the symmetries of the lattice. In presence of a magnetization along the

z -axis and spin-orbit coupling, it assumes the form

$$\varepsilon = \begin{pmatrix} \varepsilon_{xx} & \varepsilon_{xy} & 0 \\ -\varepsilon_{xy} & \varepsilon_{xx} & 0 \\ 0 & 0 & \varepsilon_{zz} \end{pmatrix}. \quad (3)$$

Taking advantage of this anti-symmetric form, the Kerr angle can be derived as:²⁶

$$\theta_K = -\frac{1}{2} \arg \left(\frac{r_+}{r_-} \right), \quad (4)$$

where r_{\pm} are the reflection coefficients given by

$$r_{\pm} = \frac{1 - n_{\mp} h(n_{\mp})}{1 + n_{\mp} h(n_{\mp})}, \quad (5)$$

in which $n_{\pm} = \sqrt{\varepsilon_{xx} \pm i\varepsilon_{xy}}$ are the refractive indexes in the circular basis and

$$h(n_{\pm}) = \frac{f(n_{\pm}) - g(n_{\pm})}{f(n_{\pm}) + g(n_{\pm})}, \quad (6)$$

$$f(n_{\pm}) = (n_{\pm} + \sqrt{\varepsilon_r}) e^{-i\frac{\omega}{c} n_{\pm} d}, \quad (7)$$

$$g(n_{\pm}) = (n_{\pm} - \sqrt{\varepsilon_r}) e^{i\frac{\omega}{c} n_{\pm} d}. \quad (8)$$

Thus, the combination of equations (3-7) permits to relate the first-principles calculations of the dielectric tensor with the Kerr angle, including the effect of a semi-infinite substrate.

Ground state properties of the chromium trihalides

Structural properties

The compounds of the CrX_3 family share many structural, electronic and magnetic properties. They have identical crystalline structure (see Fig. 1), a hexagonal lattice with point group symmetry D_{3d} .⁴⁵ The Cr atoms form a honeycomb lattice and are surrounded by

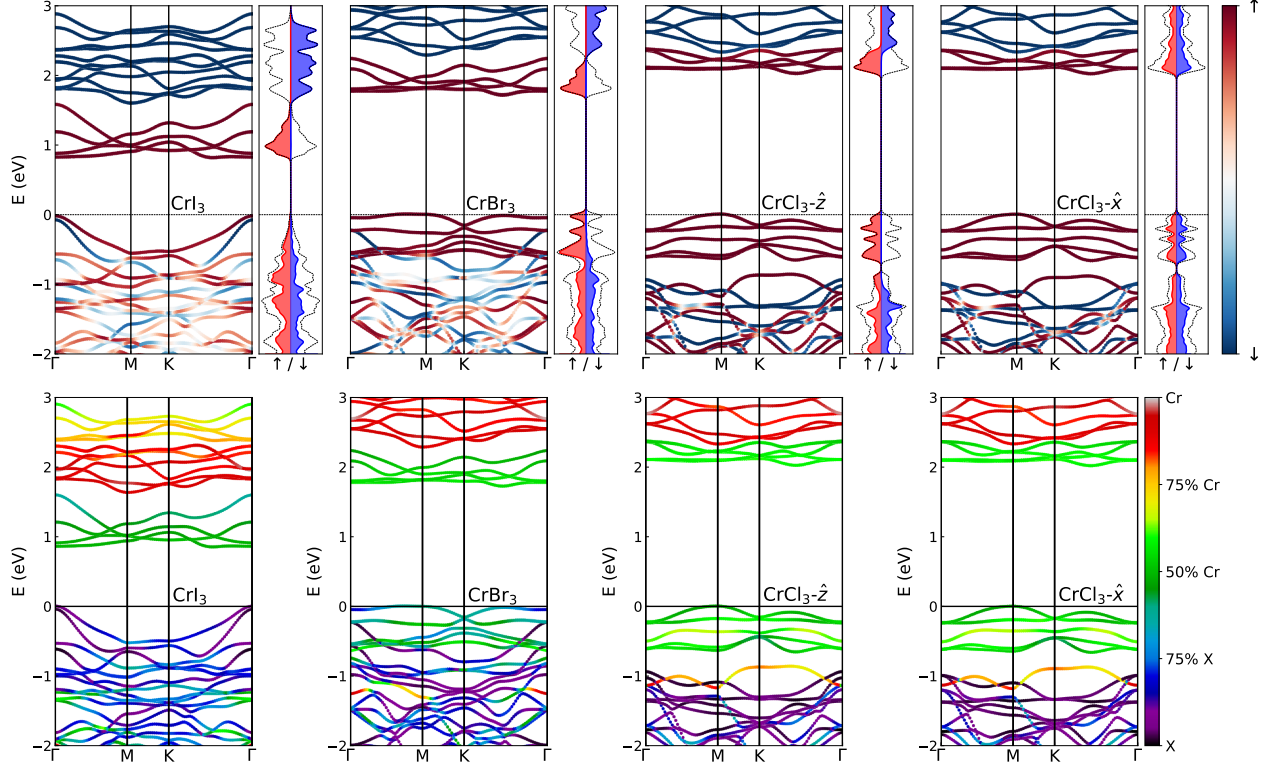


Figure 2: Upper panel. Spin-projected band structure and density of states of chromium trihalides. Red is 100 % spin-up and blue 100 % spin-down. Magnetization points in the positive z direction for the first three systems, in which case both the bands and the DOS have S_z spin projection. In the case of CrCl_3 with M along x direction, the bands are projected along S_x whereas the density of states is projected along S_z . Lower panel. Atom-projected band structures of idem materials.

the ligand's octahedron, as shown in Fig. 1d. As a result of the edge sharing geometry, first neighbor Cr atoms share a pair of ligands, providing 90° pathways for super-exchange. Moreover, the three CrX_3 compounds have ferromagnetic order down to the monolayer, with Curie temperatures of $T_I = 45K$,¹⁶ $T_{Br} = 34K$ ⁵ and $T_{Cl} = 17K$.⁷ The magnetization easy axis is off-plane for CrI_3 and CrBr_3 and in plane for CrCl_3 . Although not important in the case of monolayers, we also note that interlayer interactions in bulk are ferromagnetic for $X = I, Br$ and antiferromagnetic for $X = Cl$.⁴⁶ DFT calculations predict that, in the three compounds, the magnetic moment is hosted predominantly in the Cr ions, that have $S = 3/2$.⁴⁷

Electronic properties: a simple model

A qualitative understanding of the most salient electronic properties of the CrX_3 family is derived from the atomic model for d levels of Cr ions in the octahedral environment of the ligands. In a fully ionic picture, the nominal oxidation state of the Cr atoms is Cr^{+3} and the ligand atoms are thereby in the X^{-1} . The resulting crystal field originated by the charged Halide atoms splits the single particle d levels in an orbital triplet t_{2g} and a higher energy doublet e_g . Thus, the outermost electronic d levels of the Cr^{3+} ions are occupied by 3 electrons, that occupy the single spin t_{2g} triplet in order to minimize both orbital energy and Coulomb repulsion (intra-atomic Hund's rule). We refer to the spin channel of the occupied t_{2g} levels as *majority spin channel*. The energy arrangement of the d levels of the ionic model is shown in the scheme of Fig. 1c, and are confirmed by DFT results,⁴⁸ although the t_{2g} levels are strongly hybridized with the p bands of the ligands.

The naive ionic model predicts that the outermost shell of the X ions is a full p shell. Our DFT calculations confirm this picture. The resulting energy bands that arise from the ligand p shell and the spin majority Cr- t_{2g} coexist in energy, are strongly hybridized, and constitute the valence band of the CrX_3 family. The degree of hybridization will depend on the ligand species. On the other hand, conduction bands are spin *majority* e_g levels, hybridized with X p orbitals. The unit cell of the CrX_3 has the formula Cr_2X_6 . Therefore, there are 4 conduction bands, which are fully spin polarized. The lowest energy optical response is thus governed by transitions between the Cr- t_{2g} -X- p valence band and the Cr- e_g spin majority bands.

Electronic properties: DFT results

The band structures and density of states (DOS) of CrX_3 are presented in Fig. 2. All the calculations are done with non collinear spin-orbit coupling. The magnetization is oriented

Table 1: Summary of electronic and optical properties of CrX_3 . Bandgaps as calculated within the LDA+U and GW method. Magnetization and excitonic binding energy of first dark (E_B^d) and bright (E_B^b) excitonic state.

Material	$E_{\text{LDA+U}}$ (eV)	E_{GW} (eV)	$S_z/ S_z $	E_B^d (eV)	E_B^b (eV)
CrI_3	0.86	2.76	6.03/7.14	1.06	0.84
CrBr_3	1.75	4.45	6.00/6.68	2.05	1.99
$\text{CrCl}_3\text{-}\hat{z}$	2.04	5.47	6.00/6.44	2.62	2.57
$\text{CrCl}_3\text{-}\hat{x}$	2.09	5.47	6.00/6.44	2.63	2.57

along the z -axis for CrI_3 and CrBr_3 . In the case of CrCl_3 we consider magnetization along the x axis, given that the easy-axis of this compound is in-plane,^{7,49} and also address the case where a magnetization along the z axis is imposed. For the three materials the conduction band is formed by e_g spin majority bands, as expected from the ionic model of Fig. 1c. In the case of CrCl_3 and, to a lesser extent, CrBr_3 the valence band is dominated by the t_{2g} bands so that the energy gap is inherently related to the crystal field splitting of the $t_{2g} - e_g$ manifold in the spin majority channel. In the case of CrI_3 the top of the valence band becomes dominated by the p band of Iodine. Therefore, the band gap in CrI_3 is a metric of the inter-atomic charge transfer energy overhead. The bandgaps, as obtained with LDA+U, are summarized in Table 1. It is apparent that the bandgap correlates inversely with the nuclear charge of the ligand, resulting in a larger bandgap for lighter ligands, as evidenced in Fig. 2. As expected, the crystal field splitting follows the sequence $\Delta_{Cl} > \Delta_{Br} > \Delta_I$ on account of the larger electronegativity of lighter ligands. On the other hand, the modulus of magnetization is mainly dominated by the chromium atoms⁵⁰ and it has similar values for the three compounds, as shown in Table 1.

The spin polarization of the valence band varies from material to material, on account of the different degree of hybridization between the Cr t_{2g} spin majority levels and the p orbitals of the ligands. Thus, the spin polarization is found to be nearly 100 % spin-up for CrBr_3 and CrCl_3 .⁵¹ The stronger hybridization of Cr-I is also reflected in the absolute value of the total magnetic moment of the unit cell, shown in Table 1, indicating that each iodine ion hosts a local moment, but with antiparallel alignment among them, leading to a null

iodine moment, when summed up over the unit cell.⁵² In the case of CrCl_3 , the difference between in-plane or out-of-plane magnetization barely modifies the band dispersion.

In contrast, for the conduction bands, the e_g bands are nearly 100 % spin-up for all the compounds and with an increasing contribution from chromium d -orbitals when changing from iodine to chlorine. The implications on the optical properties of the valence band character will be discussed in the next Section. The fact that the *spin majority* e_g levels are below all the spin minority levels evidences that the crystal field splitting is smaller than the intra-atomic exchange.

Optical Properties: Dichroism and Kerr spectroscopy

From the band structures of the chromium trihalides series we can infer a strong dependence of the optical response on the ligand. Whereas the chromium atom hosts the magnetic moment, the ligand determines the strength of the spin-orbit interaction, the Cr-X hybridization of the valence band states and the magnetic anisotropy. Therefore, measuring absorbance (A) or photoluminescence (PL) of circularly polarized light, as well as Kerr angle, permits to characterize the magnitude of the magnetic anisotropy.

Excitonic effects

First, we expect strong excitonic effects on the optical properties in these 2D materials. Figure 3 shows the absorbance spectra of chromium trihalides with magnetization out-of-plane. The difference in the absorption threshold energies calculated with (solid line) and without (dashed line) excitonic effect, defines the exciton binding energy. In the figure we mark with vertical lines both the optically dark (blue dashed line) and the optically bright exciton binding energy. Values for the the bright exciton binding energy are shown in Table 1. The exciton binding energies are much higher than those of transition metal dichalcogenides.⁵³⁻⁵⁵ We attribute this enhancement to the reduced dielectric screening environment

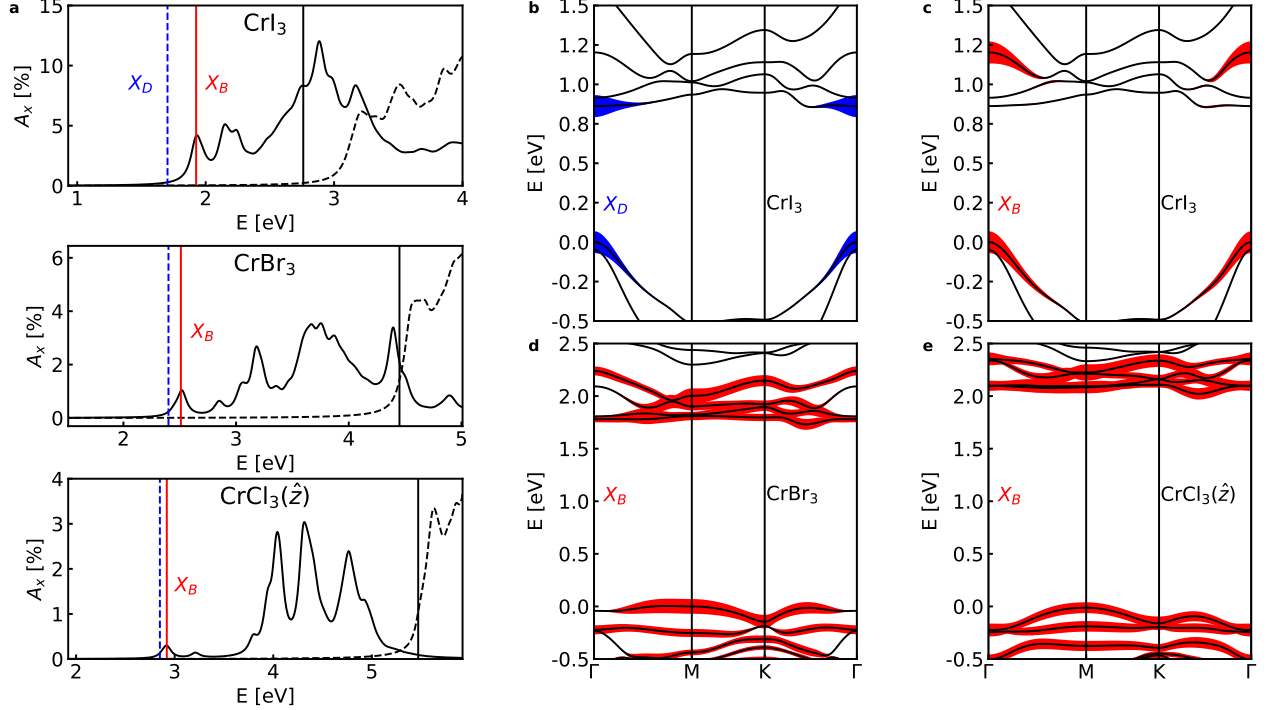


Figure 3: (a) Absorbance of linearly polarized light of chromium trihalides with magnetization out-of-plane. Solid (dashed) black lines correspond to calculations with (without) excitonic effects. Vertical lines mark the energy of first bright (red solid line) and dark (blue dashed line) exciton states together with the electronic bandgap obtained with the GW method (black solid line). (b-e) Representation of the coefficients of the wave function of relevant excitonic states: (b-c) Dark and bright excitons (X_D and X_B) of CrI_3 ; (d-e) Bright excitons of CrBr_3 and CrCl_3 , respectively.

(see supporting information).^{56–59}

The exciton binding energies are significantly higher for CrCl_3 and CrBr_3 than for CrI_3 . In order to understand this difference, we represent the electronic transitions that contribute to the main excitonic peaks, by plotting the coefficients of the exciton wave functions projected over the DFT bands in Figs. 3b-e (see refs.^{54,60,61} for details). In the case of CrI_3 , the excitonic wave function exhibits localized excitonic states in \mathbf{k} -space, which implies extended wave function in real space. In contrast, for CrBr_3 and CrCl_3 , exciton wave functions expand over the full Brillouin zone, implying an atomically localized exciton wave function. A larger localization in momentum space implies a shorter electron-hole distance in real space, and thereby, a larger exciton binding energy. The ultimate origin of this chemical trend is

probably the stronger Cr-ligand hybridization in the valence band of CrI₃. We note that our calculations set the absorbance threshold at 1.9 eV, whereas experiments found it at 1.5 eV.¹ The origin of the discrepancy is probably due to the role played by electron-lattice coupling and a possible polaronic distortion of the lattice. The very large Stokes shift observed experimentally shows that electron-lattice coupling is probably important

The height of the absorption threshold at the bright exciton peak has also a very marked dependence on the ligand: absorption is strongest for CrI₃ and weakest for CrCl₃. Given that the excitonic effect follows an inverse trend, we attribute the enhanced absorption of the CrI₃ to the large content of ligand wave function in the valence band states.

Moreover, we find as a common feature the existence of a dark ground excitonic state, clearly separated in energy (0.2 eV for CrI₃) of the first bright exciton, marked as the blue dashed line in Fig. 3. In recent experiments,⁶² the Stokes shift of PL emission is much lower in energy than the absorbance threshold. The reason is possibly the brightening of these dark excitons due to the electron-phonon coupling.

Magnetic circular dichroism and magneto-optical Kerr effect

We now consider both magnetic circular dichroism in the absorption and magneto-optical Kerr angle, which are the most common techniques to probe the magnetization of 2D chromium trihalides.^{1,16} In figure 4 we show the dichroism of the absorption coefficients, defined as:

$$\eta \equiv \frac{A_+ - A_-}{A_+ + A_-}, \quad (9)$$

for CrI₃, CrBr₃, CrCl₃, all with off-plane magnetization, and CrCi₃ with in-plane magnetization. The normalized dichroism calculated at the bright exciton energy shown in Fig. 4 also reveals a dependence on the ligand: it is slightly larger for CrI₃ than CrBr₃, and much smaller for CrCl₃ with off-plane magnetization, and almost completely negligible for in-plane magnetization. This correlates with the spin orbit coupling of the ligand, but other factors

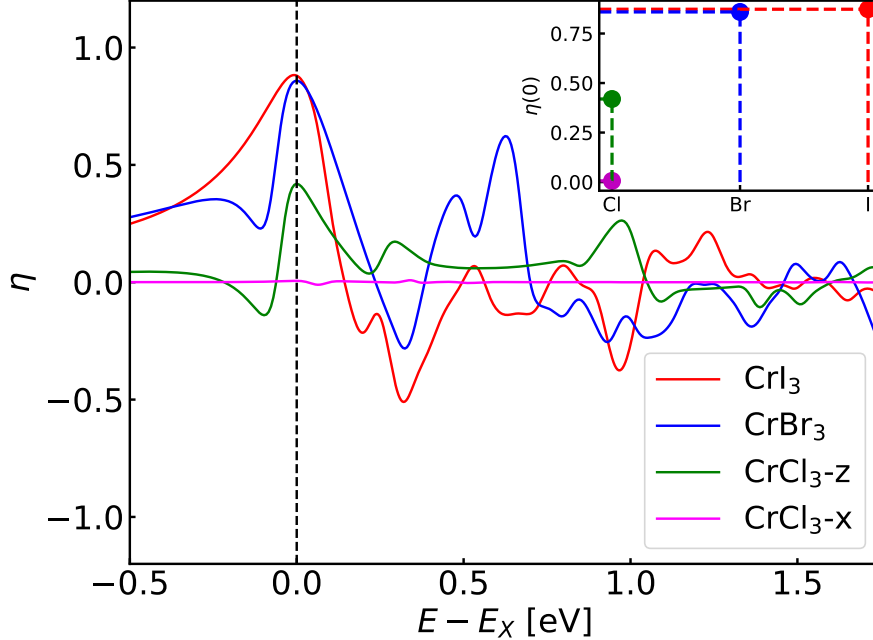


Figure 4: Magnetic circular dichroism of the absorption, as defined in eq. (9), as a function of energy, offset by the bright exciton binding energies tabulated in 1, for the three compounds. For CrCl₃ we show the case of both in-plane and off-plane magnetizations. The calculations include both the GW and excitonic contributions. In the inset we show η evaluated at the energy of the bright exciton peak.

must be at play, given the similar value obtained for CrI₃ and CrBr₃.

Our results for magneto-optical Kerr angle, θ_K , calculated including both the excitonic effects and the contribution of the substrate, are shown in figure 5(a,b,c), for the three CrX₃ compounds with off-plane magnetization. The calculation assumes that the 2D crystals have a finite thickness d , as established in eq. 3. Figure 5 summarizes the Kerr angle spectra (in mrad). We have marked with vertical lines the positive maximum of Kerr angle in each material. It is apparent that the Kerr angle threshold is an increasing function of the atomic weight of the ligand, as show in figure 5(d). This is expected since the magneto-optical Kerr effect arises as the interplay between magnetization, which is the same in the three compounds, and spin orbit coupling,⁶³ that increases for heavier ligands.

The magnitude of the Kerr angle, for the energy of the first absorption peak, computed without excitonic effect (see supplementary information), is very similar than the one ob-

tained for excitons at the bright exciton energy. We find that this rather modest excitonic enhancement is the same for the three compounds. However, as shown in Fig. 3, the excitonic correction has a dramatic impact on the location of the absorption threshold energy

We now compare our results to experimental data. The circular polarization of PL (η) in CrI_3 is 0.5 at the emission energy and the Kerr angle 8 mrad, measured at 633 nm (1.96 eV, blue-shifted 0.4 eV with respect to the absorption threshold).¹ In our calculations, our absorption threshold is shifted with respect to experiments 0.4 eV, therefore we have to compare the experimental results with the Kerr at 2.33 eV, obtaining 7 mrad. Nevertheless, the very large dependence of Kerr angle on frequency at the absorption threshold would need more experimental data for a proper comparison. In the case of CrBr_3 the polarization drops to 0.2.⁵ There are measurements of the magnetic anisotropy of CrCl_3 monolayers and few-layers but not of the Kerr angle.^{64,65} Our calculations capture the trend of the polarization and the measured Kerr angle is within the range of our simulations if the Kerr angle is measured below 2 eV.

Discussion and outlook

In this work we have employed state-of-the-art *ab initio* calculations including excitonic effects to understand optical and magnetic properties of the family of 2D chromium trihalides, CrI_3 , CrBr_3 and CrCl_3 . These three materials have the same ferromagnetic honeycomb lattice, but different ligand atoms. We have compared calculations carried out both with and without excitonic effects. We find that, for the three compounds, the exciton binding energies are much larger than the already sizeable values found in other 2D crystals, such as semiconducting transition metal dichalcogenides.⁵⁴ We find that excitons in CrI_3 are more extended, and thereby have a smaller binding energy than CrBr_3 and CrCl_3 , reflecting a larger Cr-ligand hybridization in the iodide.

Our calculations show that the two important quantities that define the magneto-optical

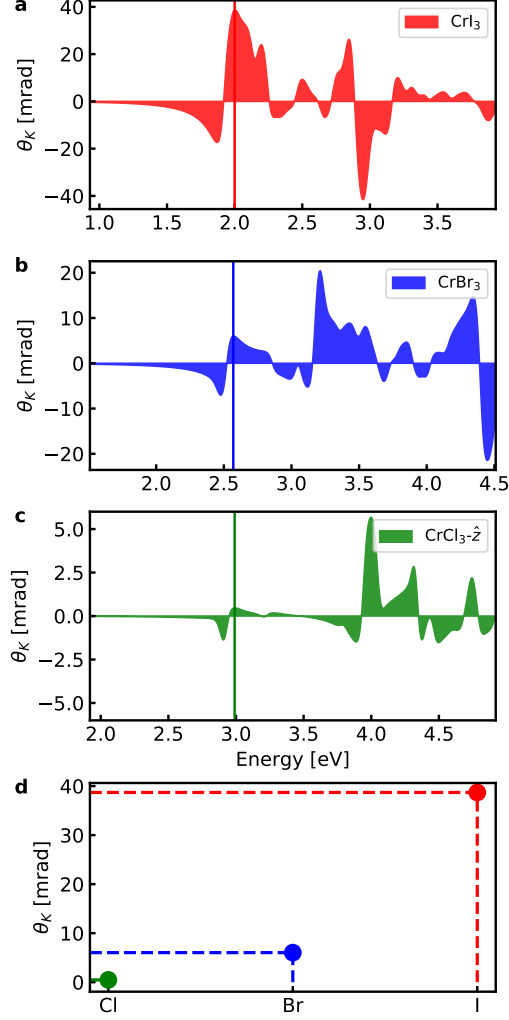


Figure 5: Kerr spectra θ_K including excitonic effects of chromium trihalides CrI_3 (red), CrBr_3 (blue) and CrCl_3 (green), all with out-of-plane magnetization. Notice the different vertical scale. Vertical lines mark the positive threshold of Kerr spectra.

response, the magnetic circular dichroism in the absorption η and the Kerr angle θ_K , have a marked dependence on the ligand. This shows that, as in the case of magnetic anisotropy,²⁷ the ligand atom affects the strength of the magneto-optical response in Cr trihalides. Thus, the chromium atom hosts the magnetization of these materials, but the magneto-optical response is controlled by the ligand.

Acknowledgements

The computations were performed on the Tirant III cluster of the Servei d'Informàtica of the University of Valencia (project vlc82) and on Mare Nostrum cluster of the Barcelona Supercomputing Center (project FI-2019-2-0034). A. M.-S. acknowledges the Marie-Curie-COFUND program Nano TRAIN For Growth II (Grant Agreement 713640). G. C. acknowledges Fundação para a Ciência e a Tecnologia (FCT) for Grant No. SFRH/BD/138806/2018. J. F.-R. acknowledges financial support from FCT for the grant UTAP-EXPL/NTec/0046/2017, as well as Generalitat Valenciana funding Prometeo 2017/139 and MINECO-Spain (Grant No. MAT2016-78625-C2). The authors acknowledge Claudia Cardoso and Nuno Peres for their contribution at the early stage of this work.

References

- (1) Huang, B.; Clark, G.; Navarro-Moratalla, E.; Klein, D. R.; Cheng, R.; Seyler, K. L.; Zhong, D.; Schmidgall, E.; McGuire, M. A.; Cobden, D. H.; Yao, W.; Xiao, D.; Jarillo-Herrero, P.; Xu, X. *Nature* **2017**, *546*, 270–273.
- (2) Klein, D. R.; MacNeill, D.; Lado, J. L.; Soriano, D.; Navarro-Moratalla, E.; Watanabe, K.; Taniguchi, T.; Manni, S.; Canfield, P.; Fernández-Rossier, J.; Jarillo-Herrero, P. *Science (New York, N.Y.)* **2018**, *360*, 1218–1222.
- (3) Gong, C.; Zhang, X. *Science (New York, N.Y.)* **2019**, *363*, 4450.
- (4) Gibertini, M.; Koperski, M.; Morpurgo, A. F.; Novoselov, K. S. *Nature Nanotechnology* **2019**, *14*, 408–419.
- (5) Zhang, Z.; Shang, J.; Jiang, C.; Rasmita, A.; Gao, W.; Yu, T. *Nano Letters* **2019**, *19*, 3138–3142.
- (6) Kim, M. et al. *Nature Electronics* **2019**, 1–7.

- (7) Cai, X.; Song, T.; Wilson, N. P.; Clark, G.; He, M.; Zhang, X.; Taniguchi, T.; Watanabe, K.; Yao, W.; Xiao, D.; McGuire, M. A.; Cobden, D. H.; Xu, X. *Nano Letters* **2019**, *19*, 3993–3998.
- (8) Gong, C.; Li, L.; Li, Z.; Ji, H.; Stern, A.; Xia, Y.; Cao, T.; Bao, W.; Wang, C.; Wang, Y.; Qiu, Z. Q.; Cava, R. J.; Louie, S. G.; Xia, J.; Zhang, X. *Nature* **2017**, *546*, 265–269.
- (9) Fei, Z.; Huang, B.; Malinowski, P.; Wang, W.; Song, T.; Sanchez, J.; Yao, W.; Xiao, D.; Zhu, X.; May, A. F.; Wu, W.; Cobden, D. H.; Chu, J.-H.; Xu, X. *Nature Materials* **2018**, *17*, 778–782.
- (10) Deng, Y.; Yu, Y.; Shi, M. Z.; Wang, J.; Chen, X. H.; Zhang, Y. *arXiv preprint arXiv:1904.11468* **2019**,
- (11) Burch, K. S.; Mandrus, D.; Park, J.-G. *Nature* **2018**, *563*, 47–52.
- (12) Cardoso, C.; Soriano, D.; García-Martínez, N.; Fernández-Rossier, J. *Physical Review Letters* **2018**, *121*, 067701.
- (13) Zollner, K.; Faria Junior, P. E.; Fabian, J. *Physical Review B* **2019**, *100*, 085128.
- (14) Li, J.; Li, Y.; Du, S.; Wang, Z.; Gu, B.-L.; Zhang, S.-C.; He, K.; Duan, W.; Xu, Y. *Science Advances* **2018**, *5*, 5685.
- (15) Sivadas, N.; Okamoto, S.; Xu, X.; Fennie, C. J.; Xiao, D. *Nano Letters* **2018**, *18*, 7658–7664.
- (16) Huang, B.; Clark, G.; Klein, D. R.; MacNeill, D.; Navarro-Moratalla, E.; Seyler, K. L.; Wilson, N.; McGuire, M. A.; Cobden, D. H.; Xiao, D.; Yao, W.; Jarillo-Herrero, P.; Xu, X. *Nature Nanotechnology* **2018**, *13*, 544–548.
- (17) Mak, K. F.; Shan, J.; Ralph, D. C. *Nature Reviews Physics* **2019**, *1*, 646–661.

- (18) Thiel, L.; Wang, Z.; Tschudin, M. A.; Rohner, D.; Gutiérrez-Lezama, I.; Ubrig, N.; Gibertini, M.; Giannini, E.; Morpurgo, A. F.; Maletinsky, P. *Science* **2019**, *364*, 973–976.
- (19) Sun, Z. et al. *Nature* **2019**, *572*, 497–501.
- (20) Mak, K. F.; Xiao, D.; Shan, J. *Nature Photonics* **2018**, *12*, 451–460.
- (21) Seyler, K. L.; Zhong, D.; Huang, B.; Linpeng, X.; Wilson, N. P.; Taniguchi, T.; Watanabe, K.; Yao, W.; Xiao, D.; McGuire, M. A.; Fu, K.-M. C.; Xu, X. *Nano Letters* **2018**, *18*, 3823–3828.
- (22) Buchner, M.; Höfler, K.; Henne, B.; Ney, V.; Ney, A. *Journal of Applied Physics* **2018**, *124*, 161101.
- (23) Argyres, P. N. *Phys. Rev.* **1955**, *97*, 334–345.
- (24) Guo, G. Y.; Ebert, H. *Phys. Rev. B* **1995**, *51*, 12633–12643.
- (25) Kumar Gudelli, V.; Guo, G.-Y. *New Journal of Physics* **2019**, *21*, 053012.
- (26) Catarina, G.; Peres, N. M. R.; Fernández-Rossier, **2019**, arXiv preprint arXiv:1910.13371.
- (27) Lado, J. L.; Fernández-Rossier, J. *2D Materials* **2017**, *4*, 035002.
- (28) Wu, M.; Li, Z.; Cao, T.; Louie, S. G. *Nature Communications* **2019**, *10*, 2371.
- (29) Torelli, D.; Olsen, T. *2D Materials* **2018**, *6*, 15028.
- (30) Torelli, D.; Thygesen, K. S.; Olsen, T. *2D Materials* **2019**, *6*, 45018.
- (31) Pervishko, A. A.; Yudin, D.; Gudelli, V. K.; Delin, A.; Eriksson, O.; Guo, G.-Y. **2019**, arXiv preprint arXiv:1909.13841.

- (32) Jang, S. W.; Jeong, M. Y.; Yoon, H.; Ryee, S.; Han, M. J. *Phys. Rev. Materials* **2019**, *3*, 031001.
- (33) Giannozzi, P. et al. *Journal of Physics: Condensed Matter* **2009**, *21*, 395502.
- (34) Baidya, S.; Yu, J.; Kim, C. H. *Physical Review B* **2018**, *98*, 155148.
- (35) Hamann, D. R. *Physical Review B* **2013**, *88*, 085117.
- (36) van Setten, M.; Giantomassi, M.; Bousquet, E.; Verstraete, M.; Hamann, D.; Gonze, X.; Rignanese, G.-M. *Computer Physics Communications* **2018**, *226*, 39–54.
- (37) Olsen, T.; Latini, S.; Rasmussen, F.; Thygesen, K. S. *Physical Review Letters* **2016**, *116*, 056401.
- (38) Marini, A.; Hogan, C.; Grüning, M.; Varsano, D. *Computer Physics Communications* **2009**, *180*, 1392–1403.
- (39) Sangalli, D. et al. *Journal of Physics: Condensed Matter* **2019**, *31*, 325902.
- (40) Larson, P.; Dvorak, M.; Wu, Z. *Physical Review B* **2013**, *88*, 125205.
- (41) Rozzi, C. A.; Varsano, D.; Marini, A.; Gross, E. K. U.; Rubio, A. *Phys. Rev. B* **2006**, *73*, 205119.
- (42) Bernardi, M.; Palummo, M.; Grossman, J. C. *Nano Letters* **2013**, *13*, 3664–3670.
- (43) Thygesen, K. S. *2D Materials* **2017**, *4*, 022004.
- (44) Constant, T. J.; Hornett, S. M.; Chang, D. E.; Hendry, E. *Nature Physics* **2016**, *12*, 124–127.
- (45) McGuire, M. A.; Dixit, H.; Cooper, V. R.; Sales, B. C. *Chemistry of Materials* **2015**, *27*, 612–620.
- (46) McGuire, M. *Crystals* **2017**, *7*, 121.

- (47) Streltsov, S. V.; Khomskii, D. I. *Physics-Uspekhi* **2017**, *60*, 1121–1146.
- (48) Soriano, D.; Cardoso, C.; Fernández-Rossier, J. *Solid State Communications* **2019**, *299*, 113662.
- (49) Wang, H.; Eyert, V.; Schwingenschlögl, U. *Journal of Physics: Condensed Matter* **2011**, *23*, 116003.
- (50) Abramchuk, M.; Jaszewski, S.; Metz, K. R.; Osterhoudt, G. B.; Wang, Y.; Burch, K. S.; Tafti, F. *Advanced Materials* **2018**, *30*, 1801325.
- (51) Zhang, W.-B.; Qu, Q.; Zhu, P.; Lam, C.-H. *J. Mater. Chem. C* **2015**, *3*, 12457–12468.
- (52) Jiang, P.; Li, L.; Liao, Z.; Zhao, Y. X.; Zhong, Z. *Nano Letters* **2018**, *18*, 3844–3849.
- (53) Molina-Sánchez, A.; Sangalli, D.; Hummer, K.; Marini, A.; Wirtz, L. *Physical Review B* **2013**, *88*, 045412.
- (54) Molina-Sánchez, A.; Hummer, K.; Wirtz, L. *Surface Science Reports* **2015**, *70*, 554–586.
- (55) Hastrup, S.; Strange, M.; Pandey, M.; Deilmann, T.; Schmidt, P. S.; Hinsche, N. F.; Gjerding, M. N.; Torelli, D.; Larsen, P. M.; Riis-Jensen, A. C.; Gath, J.; Jacobsen, K. W.; Mortensen, J. J.; Olsen, T.; Thygesen, K. S. *2D Materials* **2018**, *5*, 42002.
- (56) Qiu, D. Y.; da Jornada, F. H.; Louie, S. G. *Phys. Rev. Lett.* **2013**, *111*, 216805.
- (57) Latini, S.; Olsen, T.; Thygesen, K. S. *Phys. Rev. B* **2015**, *92*, 245123.
- (58) Noori, K.; Cheng, N. L. Q.; Xuan, F.; Quek, S. Y. *2D Materials* **2019**, *6*, 35036.
- (59) Raja, A.; Waldecker, L.; Zipfel, J.; Cho, Y.; Brem, S.; Ziegler, J. D.; Kulig, M.; Taniguchi, T.; Watanabe, K.; Malic, E.; Heinz, T. F.; Berkelbach, T. C.; Chernikov, A. *Nature Nanotechnology* **2019**, *14*, 832–837.

- (60) Paleari, F.; Galvani, T.; Amara, H.; Ducastelle, F.; Molina-Sánchez, A.; Wirtz, L. *2D Materials* **2018**, *5*, 45017.
- (61) Paleari, F.; P. C. Miranda, H.; Molina-Sánchez, A.; Wirtz, L. *Physical Review Letters* **2019**, *122*, 187401.
- (62) Seyler, K. L.; Zhong, D.; Klein, D. R.; Gao, S.; Zhang, X.; Huang, B.; Navarro-Moratalla, E.; Yang, L.; Cobden, D. H.; McGuire, M. A.; Yao, W.; Xiao, D.; Jarillo-Herrero, P.; Xu, X. *Nature Physics* **2018**, *14*, 277–281.
- (63) Qiu, Z. Q.; Bader, S. D. *Review of Scientific Instruments* **2000**, *71*, 1243–1255.
- (64) Kim, H. H. et al. *Proceedings of the National Academy of Sciences* **2019**, *116*, 11131–11136.
- (65) Wang, Z.; Gibertini, M.; Dumcenco, D.; Taniguchi, T.; Watanabe, K.; Giannini, E.; Morpurgo, A. F. *Nature Nanotechnology* **2019**,